

Stochastic FE-Analysis of Shear Localization in 2D Granular Material within a Micro-Polar Hypoplasticity

Jacek Tejchman, Jarosław Górski

Gdańsk University of Technology, Faculty of Civil and Environmental Engineering,
ul. Narutowicza 11/12, 80-952 Gdańsk, Poland, e-mails: tejchmk@pg.gda.pl, jgorski@pg.gda.pl

(Received September 15, 2006; revised December 27, 2006)

Abstract

The paper deals with investigations of the effect of the stochastic distribution of the initial void ratio in granular bodies on shear localization during shearing of an infinite granular layer 500 mm high with free dilatancy under plane strain conditions. The initial void ratio was assumed to be stochastic with a correlated random field generated by a conditional rejection method by Walukiewicz et al (1997). To simulate mechanical behaviour of a cohesionless granular material during a monotonous deformation path, a micro-polar hypoplastic constitutive law was used, which takes into account particle rotations, curvatures, non-symmetric stresses, couple stresses and the mean grain diameter as a characteristic length. The proposed model captures the salient mechanical features of granular bodies in a wide range of densities and pressures with a single set of constants. In addition, the comparative FE-analyses were carried out with a uniform and spatially non-correlated random fields of the initial void ratio.

Key words: granular material, micro-polar hypoplasticity, shear localization, correlated random field, void ratio

1. Introduction

One of the most crucial material parameters influencing the behaviour of granular bodies during different processes of flow is the initial void ratio. The effect of the mean initial void ratio on the material behaviour is well recognized. The plane strain compression experiments demonstrate that the shear resistance increases and shear zone thickness decreases with decreasing mean initial void ratio (Vardoulakis 1980, Tejchman 1989, Yoshida et al 1994, Harris et al 1995, Desrues and Viggiani 2004). In turn, the shear zone inclination relative to the direction of the minor principal stress increases with decreasing initial void ratio (Rechenmacher and Finno 2003). The position of the critical state line in void-effective stress space is not unique, depending upon deposition void ratio. Since granular materials build discrete systems composed of grains with different shape, size, roundness and roughness, the

distribution of the initial void ratio can be strongly non-uniform. Recently, Rechenmacher and Finno (2004) and Rechenmacher (2006) have shown, using a Digital Image Correlation (DIC) method, that the distribution of the void ratio is locally non-uniform along and across of the interior shear zone (a non-uniformity along the shear zone was partly also due to the presence of boundaries). Thus, not only the mean global initial void ratio, but also its initial spatial fluctuations are of major importance in order to understand the phenomenon of shear localization in granular bodies.

Different probability distributions of the initial void ratio can be assumed in granular specimens (Shahinpoor 1981, Matthies et al 1997, Gutierrez and de Borst 1998, Fenton 1999, Fenton and Griffiths 2002, Nübel 2002, Niemunis et al 2005). In general, it is not easy to assume a realistic probability distribution of the initial void ratio, due to the lack of the corresponding experimental data.

The intention of the numerical simulations is to show the effect of different probability distributions of the initial void ratio on shear localization during shearing of an infinite granular layer of sand under quasi-static plane strain conditions. By assuming periodic boundary conditions along both sides, the FE-results were independent of the layer width. Thus, it was possible to apply a minimum amount of finite elements in a horizontal direction and a large amount of small finite elements in a vertical direction. The height of the finite elements assumed was never larger than five times the mean grain diameter to capture shear localization properly (Tejchman and Bauer 1996). Finite element calculations were carried out on the basis of a micro-polar hypoplastic constitutive model (Tejchman and Gudehus 2001, Tejchman 2004a, 2006, Tejchman and Niemunis 2006) which is able to describe the essential properties of granular bodies during shear localization in a wide range of pressures and densities during monotonous deformation paths. First, the calculations were performed with a uniform probability distribution of the initial void ratio in sand for four different initial densities. Then the calculations were also carried out with different correlated random fields of the initial void ratio generated using a conditional rejection method (Walukiewicz et al 1997, Przewłócki and Górski 2001, Górski 2006). Finally, the calculations were carried out for comparative purposes with different spatially non-correlated random fields of an initial void ratio which are often applied in numerical calculations, for the sake of simplicity, to promote shear localization (Gudehus and Nübel 2004, Nübel and Karcher 1998, Leśniewska and Mróz 2003, Tejchman 2004b, Tejchman and Niemunis 2006).

The effect of the distribution of the correlated random field of the initial void ratio on shear localization has not yet been investigated in detail. Due to the lack of the experimental data, the FE-results could not be compared with any laboratory tests. However, they can constitute a basis for comparison with eventual future both laboratory experiments using a DIC (Rechenmacher 2006), PIV (Słomiński et al 2006), X-ray micro-CT technique (Sheppard et al 2006), or DEM-simulations (Cambou et al 2004, Pena et al 2005).



The present paper is organized as follows. In Section 2, a micro-polar hypoplastic model is briefly described. Section 3 deals with the simulation of discrete random fields. The information about the finite element discretisation and boundary conditions is given in Section 4. The numerical results showing the effect of different distributions of the initial void ratio on shear localization are discussed in Section 5. Finally, conclusions are given in Section 6.

2. Micro-polar Hypoplastic Model

Non-polar hypoplastic constitutive laws (Gudehus 1996, Bauer 1996, von Wolffersdorff 1996) describe the evolution of effective stress tensor depending on the current void ratio, stress state and rate of deformation by isotropic linear and non-linear tensorial functions according to the representation theorem by Wang (1970). They were formulated by a heuristic process considering the essential mechanical properties of granular materials observed with homogeneous deformations. While in hyperelastic and hypoelastic models, the constitutive equation is incrementally linear, it is incrementally non-linear in hypoplasticity. Due to the incremental non-linearity with the rate of deformation, they are able to describe both a non-linear stress-strain and volumetric behaviour of granular bodies during shearing up to and after the peak, with a single tensorial equation. They include also: barotropy (dependence on pressure level), pycnotropy (dependence on density), dilatancy and contractancy and material softening during shearing of a dense material. They are apt to describe critical states, i.e. states in which a grain aggregate can continuously be deformed at a constant stress and a constant volume under a certain rate of deformation. In contrast to elasto-plastic models, a decomposition of deformation components into elastic and plastic parts, the formulation of a yield surface, plastic potential, flow rule and hardening rule is not needed. Although, the hypoplastic models are developed without recourse to concepts of the theory of plasticity, failure surface, flow rule and plastic potential are obtained as natural outcomes. The feature of the model is a simple formulation and procedure for determination of material parameters with standard laboratory experiments. The parameters are related to granulometric properties encompassing grain-size distribution curve, shape, angularity and hardness of grains (Herle and Gudehus 1999). Owing to that, one set of material parameters is valid within a large range of pressures and densities.

A hypoplastic constitutive law cannot describe realistically shear localization, since it does not include a characteristic length of microstructure. A characteristic length can be taken into account in hypoplasticity by means of a micro-polar, non-local and second-gradient theory (Maier 2002, Tejchman 2004a). In this paper, a micro-polar theory was taken advantage of. A micro-polar model has good physical grounds, since it takes into account rotations and couple stresses which are observed during shearing, but remain negligible during homogeneous deformation (Oda 1993). Pasternak and Mühlhaus (2001) have demonstrated that the additional

rotational degree of freedom of a Cosserat continuum arises naturally by mathematical homogenization of an originally discrete system of spherical grains with contact forces and contact moments. The Cosserat model is only suitable for shear dominated problems. To describe large geotechnical problems, a micro-polar hypoplastic model has to be used with a remeshing technique or with special interface elements, due to the fact that the size of finite elements has to be sufficiently small ($< 5 \times l_c$, l_c – characteristic length) to capture properly shear localization.

A micro-polar continuum takes into account two linked levels of deformation: micro-rotation at the particle level and macro-deformation at the structural level (Schäfer 1962). Each material point has, for the case of plane strain, three degrees of freedom: two translational degrees of freedom and one independent rotational degree of freedom (Fig. 1). The gradients of the rotation are connected to curvatures which are associated with couple stresses. It leads to a non-symmetry of the stress tensor and the presence of a characteristic length.

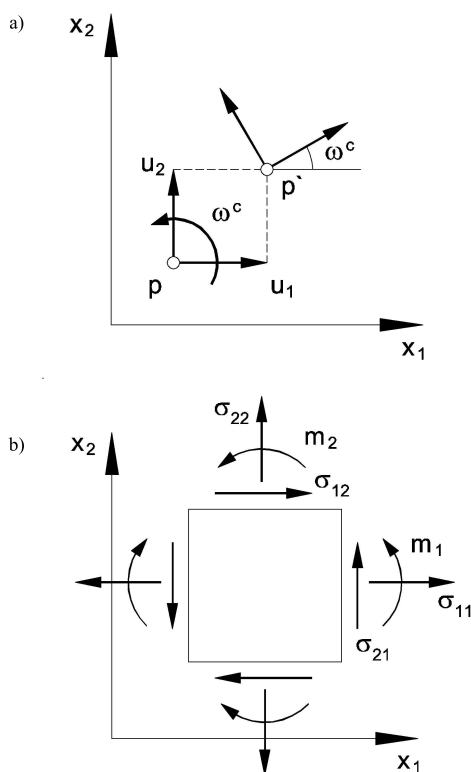


Fig. 1. Plane strain Cosserat continuum: a) degrees of freedom (u_1 – horizontal displacement, u_2 – vertical displacement, ω^c – Cosserat rotation), b) stresses σ_{ij} and couple stresses m_i at an element

The constitutive law can be summarized for plane strain as follows (Tejchman and Gudehus 2001, Tejchman 2004a, Tejchman and Niemunis 2006):

$$\dot{\sigma}_{ij} = f_s \left[L_{ij} \left(\hat{\sigma}_{kl}, \hat{m}_k, d_{kl}^c, k_k, d_{50} \right) + f_d N_{ij} \left(\hat{\sigma}_{ij} \right) \sqrt{d_{kl}^c d_{kl}^c + k_k k_k d_{50}^2} \right], \quad (1)$$

$$\hat{m}_i / d_{50} = f_s \left[L_i^c \left(\hat{\sigma}_{kl}, \hat{m}_k, d_{kl}^c, k_k, d_{50} \right) + f_d N_i^c \left(\hat{m}_i \right) \sqrt{d_{kl}^c d_{kl}^c + k_k k_k d_{50}^2} \right], \quad (2)$$

$$L_{ij} = a_1^2 d_{ij}^c + \hat{\sigma}_{ij} \left(\hat{\sigma}_{kl} d_{kl}^c + m_k k_k d_{50} \right), \quad (3)$$

$$L_i^c = a_1^2 k_i d_{50} + a_1^2 \hat{m}_i \left(\hat{\sigma}_{kl} d_{kl}^c + \hat{m}_k k_k d_{50} \right), \quad (4)$$

$$N_{ij} = a_1 \left(\hat{\sigma}_{ij} + \hat{\sigma}_{ij}^* \right), \quad (5)$$

$$N_i^c = a_1^2 a_c \hat{m}_i, \quad (6)$$

$$\hat{\sigma}_{ij} = \frac{\sigma_{ij}}{\sigma_{kk}}, \quad (7)$$

$$\hat{m}_i = \frac{m_i}{\sigma_{kk} d_{50}}, \quad (8)$$

$$\dot{\sigma}_{ij} = \dot{\sigma}_{ij} - w_{ik} \sigma_{kj} + \sigma_{ik} w_{kj}, \quad (9)$$

$$\dot{\hat{m}}_i = \dot{\hat{m}}_i - 0.5 w_{ik} m_k + 0.5 m_k w_{ki}, \quad (10)$$

$$d_{ij} = \frac{v_{i,j} + v_{j,i}}{2}, \quad w_{ij} = \frac{v_{i,j} - v_{j,i}}{2}, \quad (11)$$

$$d_{ij}^c = d_{ij} + w_{ij} - w_{ij}^c, \quad k_i = w_{,i}^c, \quad (12)$$

$$w_{kk}^c = 0, \quad w_{21}^c = -w_{12}^c = w^c, \quad (13)$$

$$\dot{e} = (1 + e) d_{kk}, \quad (14)$$

$$e_i = e_{i0} \exp \left[- \left(- \frac{\sigma_{kk}}{h_s} \right)^n \right], \quad (15)$$



$$e_d = e_{d0} \exp \left[- \left(- \frac{\sigma_{kk}}{h_s} \right)^n \right], \quad (16)$$

$$e_c = e_{c0} \exp \left[- \left(- \frac{\sigma_{kk}}{h_s} \right)^n \right], \quad (17)$$

$$f_s = \frac{h_s}{nh_i} \left(\frac{1 + e_i}{e_i} \right) \left(\frac{e_i}{e} \right)^\beta \left(- \frac{\sigma_{kk}}{h_s} \right)^{1-n}, \quad (18)$$

$$h_i = \frac{1}{c_1^2} + \frac{1}{3} - \left(\frac{e_{i0} - e_{d0}}{e_{c0} - e_{d0}} \right)^\alpha \frac{1}{c_1 \sqrt{3}}, \quad (19)$$

$$f_d = \left(\frac{e - e_d}{e_c - e_d} \right)^\alpha, \quad (20)$$

$$a_1^{-1} = c_1 + c_2 \sqrt{\hat{\sigma}_{kl}^* \hat{\sigma}_{lk}^*} [1 + \cos(3\theta)], \quad (21)$$

$$\cos(3\theta) = - \frac{\sqrt{6}}{[\hat{\sigma}_{kl}^* \hat{\sigma}_{kl}^*]^{1.5}} \hat{\sigma}_{kl}^* \hat{\sigma}_{lm}^* \hat{\sigma}_{mk}^*, \quad (22)$$

$$c_1 = \sqrt{\frac{3}{8}} \frac{(3 - \sin \phi_c)}{\sin \phi_c}, \quad c_2 = \frac{3}{8} \frac{(3 + \sin \phi_c)}{\sin \phi_c}, \quad (23)$$

wherein:

- a_c – micro-polar constant,
- a_1 – parameter representing the deviatoric part of the normalized stress in critical states (Bauer 1996),
- d_{ij}^c – polar rate of deformation tensor,
- d_{kl} – rate of deformation tensor (stretching tensor),
- d_{50} – mean grain diameter,
- e – current void ratio,
- e_c – critical void ratio (e_{c0} – value of e_c for $\sigma_{kk} = 0$),
- e_d – void ratio at maximum densification (e_{d0} – value of e_d for $\sigma_{kk} = 0$),
- e_i – maximum void ratio (e_{i0} – value of e_i for $\sigma_{kk} = 0$),
- f_d – density factor,
- f_s – stiffness factor,
- h_s – granulate hardness,
- k_i – rate of curvature vector,
- m_i – Cauchy couple stress vector,



- $\overset{\circ}{m}_i$ – Jaumann couple stress rate vector (objective couple stress rate vector),
- n – compression coefficient,
- v – material velocity,
- w^c – rate of Cosserat rotation,
- w_{ij} – spin tensor,
- α – pycnotropy coefficient,
- β – stiffness coefficient,
- θ – Lode angle,
- ϕ_c – critical angle of internal friction during stationary flow,
- σ_{ij} – Cauchy stress tensor,
- σ_{ij}^* – deviatoric part of σ_{ij} ,
- $\overset{\circ}{\sigma}_{ij}$ – Jaumann stress rate tensor (objective stress rate tensor),
- σ_{kk} – mean stress.

A micro-polar parameter a_c can be correlated with the grain roughness with the aid of a numerical analysis for shearing of a narrow granular strip between two very rough boundaries (Tejchman and Gudehus 2001). It can be represented by a constant value of a_c (e.g. $a_c = 1 \div 5$). In this case, the function $N_i^c = (1 \div 5)a_1^2 \hat{m}_i$ (Eq. 6). It can also be connected to the parameter a_1 (e.g. $a_c = (0.5 \div 1.5) \times a_1^{-1}$). In this case, the function $N_i^c = (0.5 \div 1.5)a_1 \hat{m}_i$ (Eq. 6). The parameter a_1^{-1} is equal to 3.0–4.3 for the usual critical friction angles of granulates.

The constitutive relationship requires the following ten material constants: $e_{i0}, e_{d0}, e_{c0}, \phi_c, h_s, \beta, n, \alpha, a_c$ and d_{50} . The parameters h_s and n are estimated from a single oedometric compression test with an initially loose specimen (h_s reflects the slope of the curve in a semi-logarithmic representation, and n its curvature). The constants α and β are found from a triaxial or plane strain test with a dense specimen and trigger the magnitude and position of the peak friction angle. The angle ϕ_c is determined from the angle of repose, or measured in a triaxial test with a loose specimen. The values of e_{i0}, e_{d0}, e_{c0} and d_{50} are obtained with conventional index tests ($e_{c0} \approx e_{\max}, e_{d0} \approx e_{\min}, e_{i0} \approx (1.1 \div 1.5)e_{\max}$). The FE-analyses were carried out with the material constants for so-called Karlsruhe sand (Tejchman and Gudehus 2001): $e_{i0} = 1.30, e_{d0} = 0.51, e_{c0} = 0.82, \phi_c = 30^\circ, h_s = 190$ MPa, $\beta = 1, n = 0.50, \alpha = 0.30, a_c = a_1^{-1}$ and $d_{50} = 0.5$ mm.

3. Simulation of Correlated Random Fields

A correlated random field of the initial void ratio e_o was assumed in the form of a two-dimensional Gaussian random field. The midpoint method was applied. The method approximated the random field in each finite element by a single random variable defined as the value of the field at its centre. Randomness of the initial void



ratio was described by the following homogeneous covariance function (Przewłócki and Górski 2001)

$$K(x_1, x_2) = s_d^2 \times e^{-\lambda_{x_1} \Delta x_1} (1 + \lambda_{x_1} \Delta x_1) \times e^{-\lambda_{x_2} \Delta x_2} (1 + \lambda_{x_2} \Delta x_2), \quad (24)$$

where Δx_1 and Δx_2 are the distances between two field points along the axes x_1 and x_2 , λ_{x_1} and λ_{x_2} are the decay coefficients characterizing a spatial variability of the specimen properties while the standard deviation s_d represents their scattering. Random fields in the amount of 2000 were generated using a conditional rejection method proposed by Walukiewicz et al (1997). A discrete random field was described by multidimensional random variables defined at mesh nodes. The field was represented by the random vector $\mathbf{x}(m \times 1)$, and its mean value $\bar{\mathbf{x}}(m \times 1)$. The covariance function was replaced by the symmetric and positively defined covariance matrix $\mathbf{K}(m \times m)$. The random variable vector $\mathbf{x}(m \times 1)$ was divided into blocks consisting of the unknown $\mathbf{x}_u(n \times 1)$ and the known $\mathbf{x}_k(p \times 1)$ elements ($n + p = m$). The covariance matrix $\mathbf{K}(m \times m)$ and the expected values vector $\bar{\mathbf{x}}(m \times 1)$ were also appropriately split:

$$\mathbf{x} = \left\{ \begin{array}{c} \mathbf{x}_u \\ \mathbf{x}_k \end{array} \right\} \begin{array}{c} n \\ p \end{array}, \quad \mathbf{K} = \left[\begin{array}{cc} \mathbf{K}_{11} & \mathbf{K}_{12} \\ \mathbf{K}_{21} & \mathbf{K}_{22} \end{array} \right] \begin{array}{c} n \\ p \end{array}, \quad \bar{\mathbf{x}} = \left\{ \begin{array}{c} \bar{\mathbf{x}}_u \\ \bar{\mathbf{x}}_k \end{array} \right\} \begin{array}{c} n \\ p \end{array}. \quad (25)$$

The unknown vector \mathbf{x}_u was estimated from the following conditional truncated distribution

$$f_t \left(\begin{array}{c} \mathbf{x}_u \\ \mathbf{x}_k \end{array} \right) = (1 - t)^{-m/2} (\det \mathbf{K}_c)^{-1/2} (2\pi)^{-m/2} \times \exp \left(-\frac{1}{2(1-t)} (\mathbf{x}_u - \bar{\mathbf{x}}_c)^T \mathbf{K}_c^{-1} (\mathbf{x}_u - \bar{\mathbf{x}}_c) \right), \quad (26)$$

where \mathbf{K}_c and $\bar{\mathbf{x}}_c$ are described as the conditional covariance matrix and conditional expected value vector:

$$\mathbf{K}_c = \mathbf{K}_{11} - \mathbf{K}_{12} \mathbf{K}_{22}^{-1} \mathbf{K}_{21}, \quad (27)$$

$$\bar{\mathbf{x}}_c = \bar{\mathbf{x}}_u + \mathbf{K}_{12} \mathbf{K}_{22}^{-1} (\mathbf{x}_k - \bar{\mathbf{x}}_k). \quad (28)$$

The constant t is the truncation parameter

$$t = \frac{s_d \exp \left(-\frac{s_d^2}{2} \right)}{\sqrt{2\pi} \operatorname{erf}(s_d)} \quad (29)$$

with



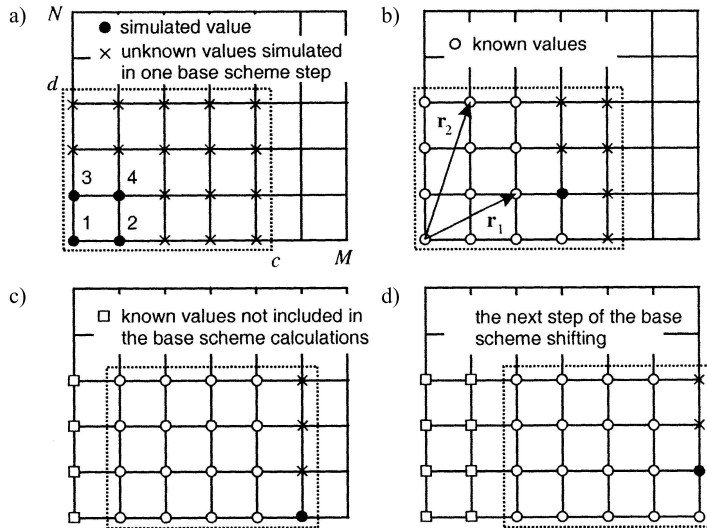


Fig. 2. Successive coverage of field points with a moving propagation scheme (Górski 2006)

$$\text{erf}(s_d) = \frac{1}{\sqrt{2\pi}} \int_0^{s_d} \exp\left(-\frac{x^2}{2}\right) dx. \quad (30)$$

Generally, the single variable was determined in accordance with the random field boundaries

$$x_i = a_i + (b_i - a_i) u_i, \quad i = 1, \dots, m, \quad (31)$$

where u_i are the random variables uniformly distributed in the interval $[0,1]$, and (a_i, b_i) , $i = 1, 2, \dots, m$ are intervals of the reals (an envelope of the random field). The parameters (a_i, b_i) can be related to the standard deviation s_d . Here, to generate the initial void ratio, the following field boundaries are assumed: $a_i, b_i = e_o \mp 6s_d$, where $e_o = 0.60$ (dense sand). It should be pointed out that the void ratio scattering in the specimen was also limited by the pressure dependent void ratios e_{i0} (upper bound) and e_{d0} (lower bound), Eqs. (15 and 16), which are essential for large standard deviations.

The simulation process was divided into three stages. First, the four corner random values were generated. Next, a propagation scheme with a growing number of points covered a defined base scheme of the field mesh. In the third stage, the base scheme was appropriately shifted, and the next group of unknown random values was simulated (Fig. 2). The base scheme was translated so as to cover all the field nodes.

For the sake of simplicity and for a significant reduction of the computation time, only single realizations of the random correlated fields were performed. A calculation of a sufficient number of nonlinear realizations which can guarantee the convergence of the outputs is at present impossible due to a limited computer capacity. In the next working steps, selected representative random fields will be chosen using the idea of the stratified sampling (Rubinstein 1981) or the Latin hypercube sampling method (Florian 1992, Vorechovsky and Matesova 2006) which feature is that the joint probability distribution functions for random variables are divided into intervals with equal probability.

In addition, three different spatially non-correlated distributions of the initial void ratio were assumed. In the first case, the initial void ratio e_o was randomly distributed by means of a random generator in such a way that the initial void ratio was increased in every element layer by the value $a \times r$, where a is a constant and r is a random number between 0 and 1 (Tejchman 2004b). Thus, the fluctuating initial void ratio in an initially dense specimen with the mean value of 0.60 was equal to

$$e_o = 0.55 + 0.1r \quad \text{or} \quad e_o = 0.50 + 0.2r. \quad (32)$$

In the second case, the spatially fluctuating initial void ratio e was calculated from the formula given by Shahinpoor (1981), Nübel and Karcher (1998), Gudehus and Nübel (2004), Tejchman and Niemunis (2006):

$$e = -\frac{1}{\xi} \ln [(1-r) \exp(-\xi e_m) + r \exp(-\xi e_M)], \quad (33)$$

wherein the parameters are: $\xi = 1.0$ (for the mean void ratio of 0.60), $e_m = 0.001$ and $e_M = 1.641$. Eq. 33 has been derived analogously to the partition function of statistical mechanics, however, imposing bounds e_m and e_M upon the size of the individual Voronoi cells. The deviation of the distribution of void ratio increases with decreasing number of voids (grains) in a volume element and decreasing mean global void ratio of the specimen. Since the area of each finite element was $5d_{50} \times 5d_{50}$, the initial void ratio in each element was assumed as the mean value of 25 random values calculated by Eq. 33.

In the third case, a Gaussian distribution of e_o was used using a polar form of the so-called Box-Muller transformation (Box and Muller 1958, Tejchman 2006). One assumed the mean value of the initial void ratio $\bar{e}_0 = 0.60$ with a standard deviation of $s_d = 0.05$ or 0.20 and a cut-off of ± 0.3 .

The calculations of a stochastic size effect were carried out for two different decay coefficients: $\lambda_{x1} = 1$ (strongly correlated field) or $\lambda_{x1} = 3$ (weakly correlated field) and two different standard deviations 0.05 and 0.2. The initial void ratio e_o was distributed in two ways. In the first case, the same initial void ratio was assumed in each triangular element belonging to the quadrilateral (so-called approach 'A').

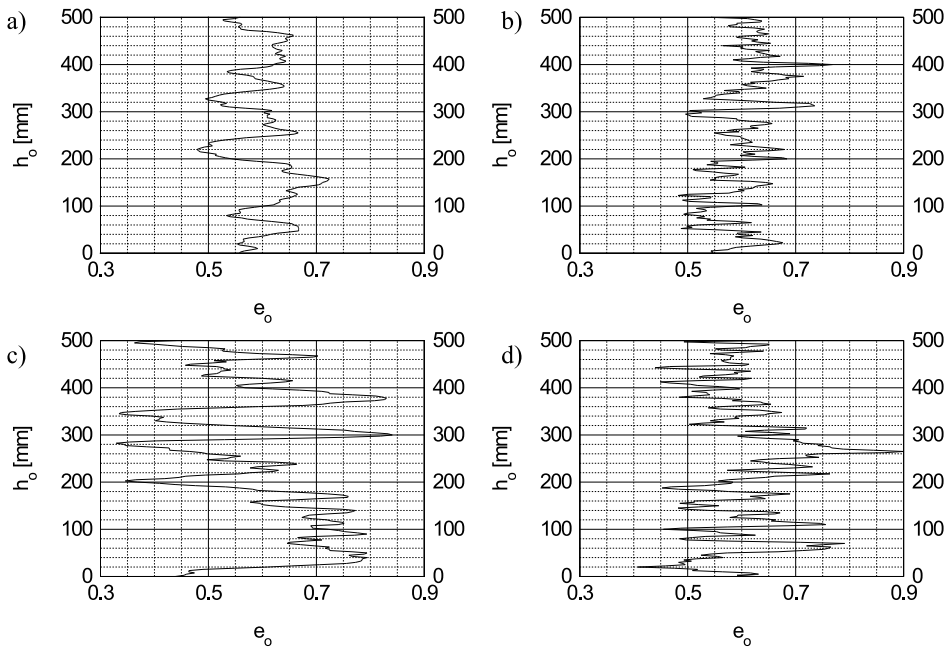


Fig. 3. Distribution of correlated random field of initial void ratio along the layer height $h_o = 500$ mm (approach 'A'): a) $\bar{e}_o = 0.60$, $s_d = 0.05$, $\lambda_{x2} = 1$, b) $\bar{e}_o = 0.60$, $s_d = 0.05$, $\lambda_{x2} = 3$, c) $\bar{e}_o = 0.60$, $s_d = 0.2$, $\lambda_{x2} = 1$, d) $\bar{e}_o = 0.60$, $s_d = 0.2$, $\lambda_{x2} = 3$

Only one-dimensional random field was generated (one assumed $\Delta x_1 = 0$ and the value of the decay coefficient λ_{x1} in the x_1 direction turned out to be unimportant in Eq. 24), and the initial void ratio was the same in a horizontal direction x_1 .

In addition, the different initial void ratio was calculated for all individual triangular finite elements (so-called approach 'B') to check the effect of horizontal imperfections on the material behaviour. As the two-dimensional random field was applied, the initial void ratio was assumed to vary also in a horizontal direction along x_1 (the correlation distance was $\Delta x_1 = 2.5$ mm in Eq. 24). By assuming such small changes of e_o in a horizontal direction, the results were only insignificantly affected by the layer width. These comparative calculations were performed with the same layer widths and heights as in the case of the method 'A'.

Figures 3 and 4 show some single random distributions of e_o generated initially for simulations.

4. FE-input Data

FE-calculations of plane strain simple shearing under vertical pressure with free dilatancy (Tejchman and Gudehus 2001) were performed for an infinite granular layer with a height of $h_o = 500$ mm. For this height, the thickness of the shear zone does not certainly depend on the specimen size (Tejchman and Gudehus 2001).

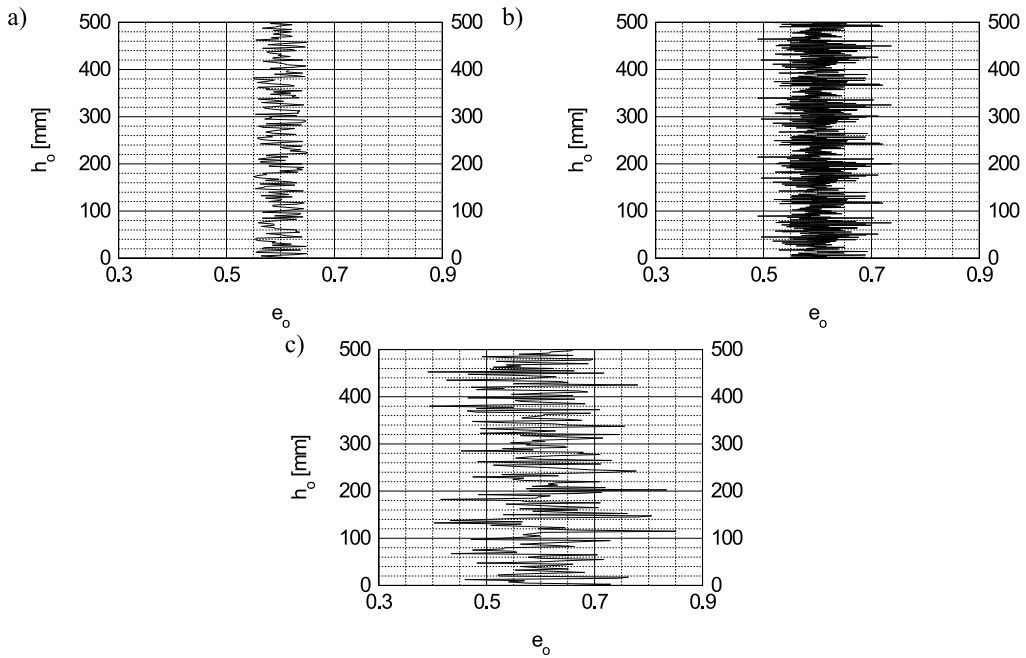


Fig. 4. Distribution of spatially non-correlated initial void ratio along the layer height $h_o = 500$ mm: a) $e_o = 0.55 + 0.1r$, b) non-correlated Gaussian ($\bar{e}_o = 0.60, s_d = 0.05$), c) by Shahinpoor (1981) ($\bar{e}_o = 0.60$)

Quadrilateral finite elements composed of four diagonally crossed triangles were applied to avoid volumetric locking (Groen 1997). The calculations were performed with a section of an infinite shear layer with a width of $b = h_o$, discretised by 200 quadrilateral elements. The height of the elements was always $5 \times d_{50}$ to obtain mesh-independent results (Tejchman and Bauer 1996). The behaviour of an infinite shear layer is modelled by lateral boundary conditions, i.e. displacements and rotations along both sides of the column are constrained by the same amount (Tejchman and Gudehus 2001). Consequently, the evolution of state quantities is independent of the direction of shearing if an initially homogeneous state is considered. The integration was performed with three sampling points placed in the middle of each element side. Linear shape functions for displacements and the Cosserat rotation were used. The calculations were carried out with large deformations and curvatures using the so-called updated Lagrange formulation, i.e. by updating the element geometry and element volume after each integration step. As the initial stress state in the granular strip, a K_o -state without polar quantities ($\sigma_{22} = -1.0$ kPa, $\sigma_{11} = \sigma_{33} = -0.3$ kPa, $\sigma_{12} = \sigma_{21} = m_1 = m_2 = 0$) was assumed (σ_{11} – horizontal normal stress, σ_{22} – vertical normal stress, σ_{33} – horizontal normal stress perpendicular to the plane of deformation, σ_{12} – horizontal shear stress, σ_{21} –



vertical shear stress, m_1 – horizontal couple stress, m_2 – vertical couple stress, Fig. 1b). The influence of the gravity was neglected.

A quasi-static shear deformation was initiated through constant horizontal displacement increments Δu prescribed at the nodes along the top of the layer ($\Delta u/h_o = 0.000001$). Both bottom and top surfaces were assumed to be very rough, i.e. sliding and rotation of particles against the bounding surface were excluded. The boundary conditions were along the bottom: $u_1 = 0$, $u_2 = 0$ and $\omega^c = 0$, and along the top: $u_1 = n\Delta u$, $\omega^c = 0$, and $\sigma_{22} = p$. The index '1' denotes the co-ordinate in the direction of shearing, and the index '2' denotes the co-ordinate normal to the direction of shearing, n is the number of time steps ($n = 20000$), Δu is the constant displacement increment in one step and p denotes the prescribed vertical surface pressure, which was kept constant along the top of the layer. The vertical pressures were assumed to be $p = 200$ kPa.

For the solution of the non-linear equation system, a modified Newton-Raphson scheme with line search was used. The global stiffness matrix was calculated with only two first terms of the constitutive equations. The stiffness matrix was updated every 100 steps. To accelerate the calculations, the initial increments of displacements and Cosserat rotations during shearing in one direction were assumed to be equal to the converged incremental nodal displacement and rotation solutions from the previous step. The iteration steps were performed using translational and rotational convergence criteria. For the time integration of stresses and couple stresses in finite elements, a one-step Euler forward scheme was applied.

5. FE-results

5.1. Uniform Distribution of the Initial Void Ratio

Figs. 5–8 show calculations results for a sand layer with different uniform initial void ratios in the range of 0.60–0.90. Fig. 5 presents the evolution of the mobilized internal friction angle $\phi = \arctan(\sigma_{12}/\sigma_{22})$ against the normalized horizontal displacement of the top boundary u_1^t/h_o . The mobilized friction angle ϕ is related to the entire granular layer since the stresses σ_{12} and σ_{22} are independent of both the height and length of the layer. The deformed FE-meshes at residual state are shown in Fig. 6. In turn, Fig. 7 presents the distribution of the Cosserat rotation ω^c and void ratio e across the normalized height x_2/d_{50} . The relationship between the thickness of the shear zone t_s and initial void ratio e_o is demonstrated in Fig. 8.

All state variables (stress, couple stress, mobilized friction angle and void ratio) tend to asymptotic values. The mobilized internal friction angle for dense and medium dense sand ($e_o \leq 0.80$) increases, shows a peak and decreases later. For loose sand ($e_o = 0.90$), it does not indicate any peak. The mobilized friction angle at peak ϕ_p decreases obviously with increasing e_o : $\phi_p = 45.1^\circ$ ($e_o = 0.60$), $\phi_p = 37.0^\circ$ ($e_o = 0.70$) and $\phi_p = 31.3^\circ$ ($e_o = 0.80$). The residual friction angle similarly

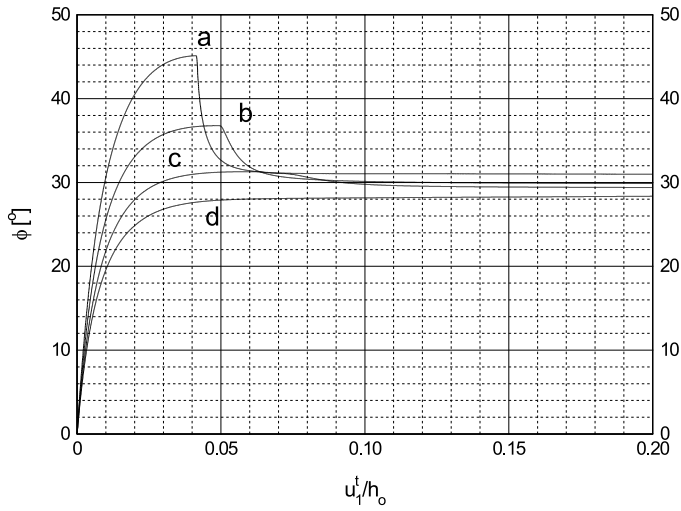


Fig. 5. Evolution of mobilized internal friction angle ϕ versus u_1^t/h_o during shearing with uniform distribution of the initial void ratio: a) $e_o = 0.60$, b) $e_o = 0.70$, c) $e_o = 0.80$, d) $e_o = 0.90$

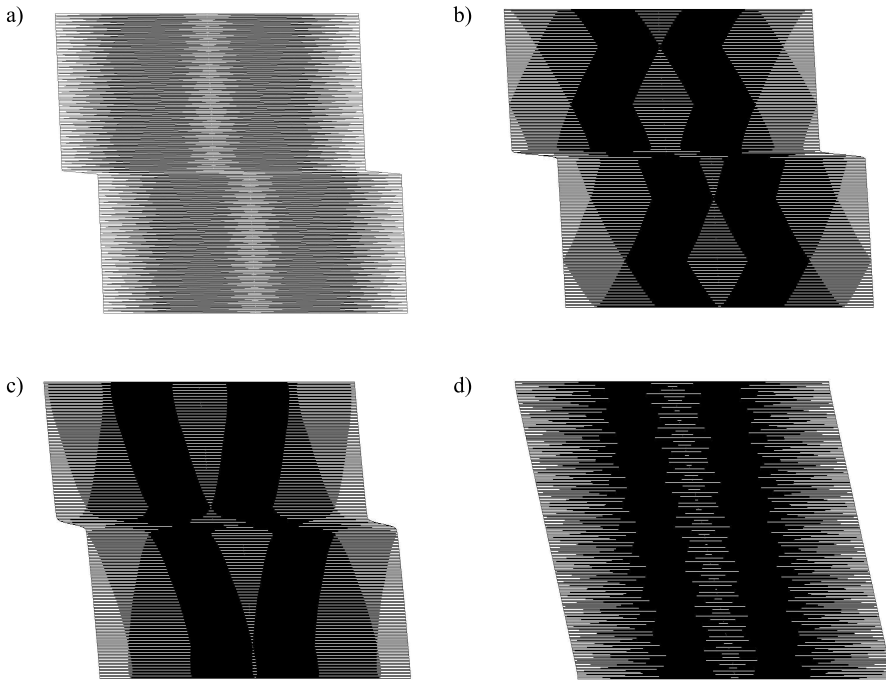


Fig. 6. Deformed FE-meshes at residual state during shearing with uniform distribution of the initial void ratio: a) $e_o = 0.60$, b) $e_o = 0.70$, c) $e_o = 0.80$, d) $e_o = 0.90$



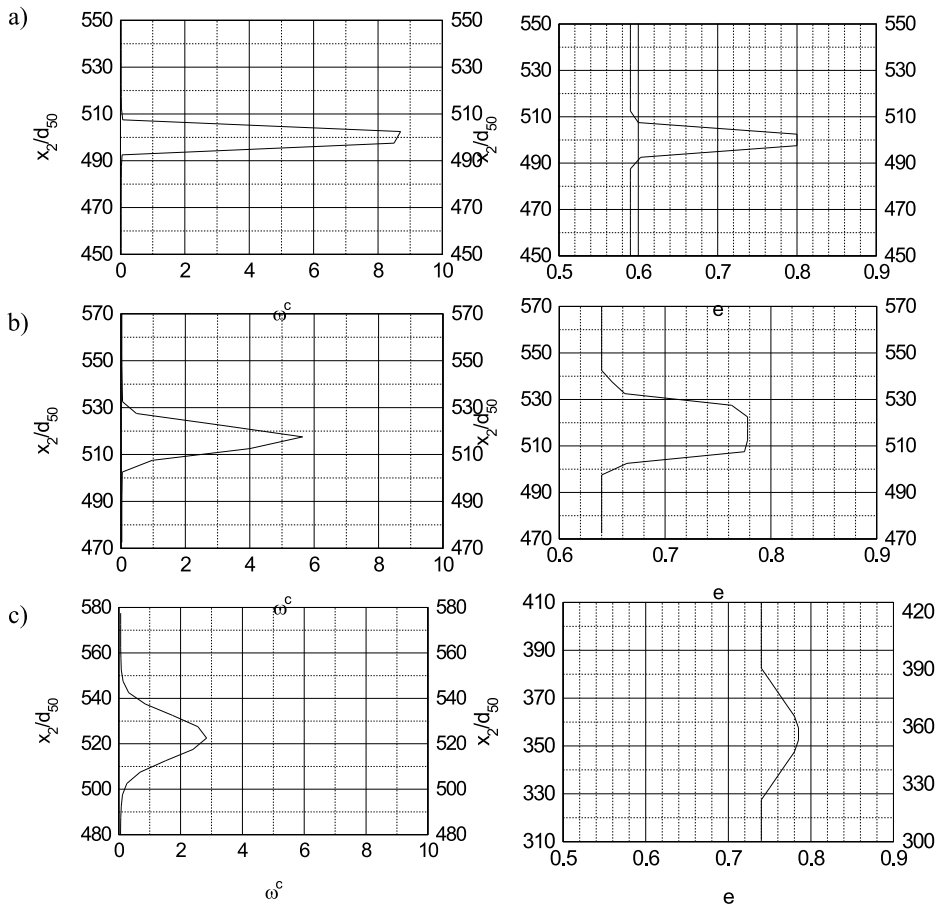


Fig. 7. Distribution of Cosserat rotation ω^c and void ratio e across the normalized height x_2/d_{50} at residual state with uniform distribution of the initial void ratio: a) $e_o = 0.60$, b) $e_o = 0.70$, c) $e_o = 0.80$

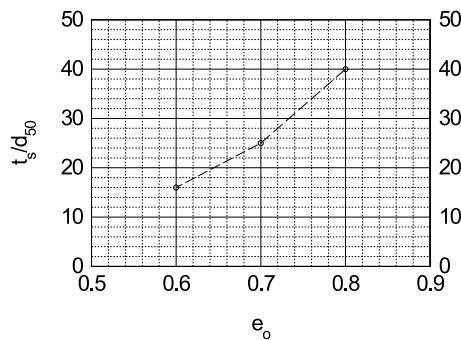


Fig. 8. Relationship between normalized shear zone thickness t_s/d_{50} at residual state and initial void ratio e_o in the range 0.60–0.80 (uniform distribution of the initial void ratio)

behaves: $\phi_{cr} = 31^\circ$ ($e_o = 0.60$), $\phi_{cr} = 30.0^\circ$ ($e_o = 0.70$), $\phi_{cr} = 29.4^\circ$ ($e_o = 0.80$) and $\phi_p = 28.4^\circ$ ($e_o = 0.90$ mm).

The width of the shear zone appearing inside the layer (characterized among others by the presence of Cosserat rotation, Fig. 7) almost linearly increases with increasing e_o : $16 \times d_{50}$ ($e_o = 0.60$), $25 \times d_{50}$ ($e_o = 0.70$ mm) and $40 \times d_{50}$ ($e_o = 0.80$ mm), (Fig. 8). If the initial void ratio is larger than the pressure-dependent critical void ratio by Eq. 17 ($e_o = 0.90 > e_c$), the width of the shear zone is equal to the layer height $1000 \times d_{50}$ (Fig. 6d). The void ratio reaches in the shear zone (Fig. 7) a pressure dependent value depicted by Eq. 17.

5.2. Correlated Random Fields of the Initial Void Ratio

The FE-results for single realizations with a spatially distribution of the initial void ratio are shown in Figs. 9–13.

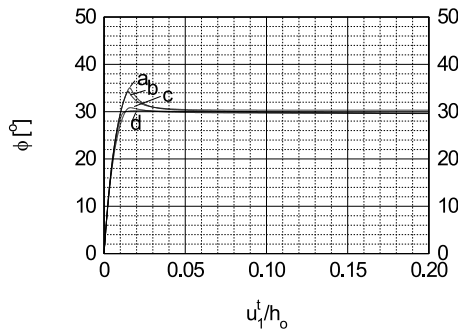


Fig. 9. Evolution of mobilized internal friction angle ϕ versus u_1^t/h_o during shearing with dense sand (correlated random field of e_o , approach 'A'): a) $\bar{e}_o = 0.60$, $s_d = 0.05$, $\lambda_{x2} = 1$, b) $\bar{e}_o = 0.60$, $s_d = 0.05$, $\lambda_{x2} = 3$, c) $\bar{e}_o = 0.60$, $s_d = 0.2$, $\lambda_{x2} = 1$, d) $\bar{e}_o = 0.60$, $s_d = 0.2$, $\lambda_{x2} = 3$

In the case of approach 'A' ($\Delta x_1 = 0$ in Eq. 24), the mobilized friction angle at peak decreases with increasing decay coefficient λ_{x2} and standard deviation s_d (Fig. 9): $\phi_p = 35.1^\circ$ ($\lambda_{x2} = 1$, $s_d = 0.05$), $\phi_p = 34.3^\circ$ ($\lambda_{x2} = 3$, $s_d = 0.05$), $\phi_p = 30.8^\circ$ ($\lambda_{x2} = 1$, $s_d = 0.2$) and $\phi_p = 30.2^\circ$ ($\lambda_{x2} = 3$, $s_d = 0.2$). Thus, it is significantly smaller than this with the uniform distribution of $e_o = 0.60$ ($\phi_p = 45.1^\circ$). In turn, the residual friction angle is similar, about $\phi_{res} = 30^\circ$.

During initial shearing, several parallel shear zones again occur (Fig. 10). Next, only one develops horizontally at the weakest spot. The thickness of the shear zone mainly decreases with increasing λ_{x2} and s_d : $30 \times d_{50}$ ($\lambda_{x2} = 1$, $s_d = 0.05$), $22 \times d_{50}$ ($\lambda_{x2} = 3$, $s_d = 0.05$), $30 \times d_{50}$ ($\lambda_{x2} = 1$, $s_d = 0.2$) and $30 \times d_{50}$ ($\lambda_{x2} = 3$, $s_d = 0.2$), Fig. 11.

In the case of the approach 'B' ($\Delta x_1 \neq 0$ in Eq. 24), the mobilized friction angle at peak is higher and the residual mobilized friction angle is similar as compared to

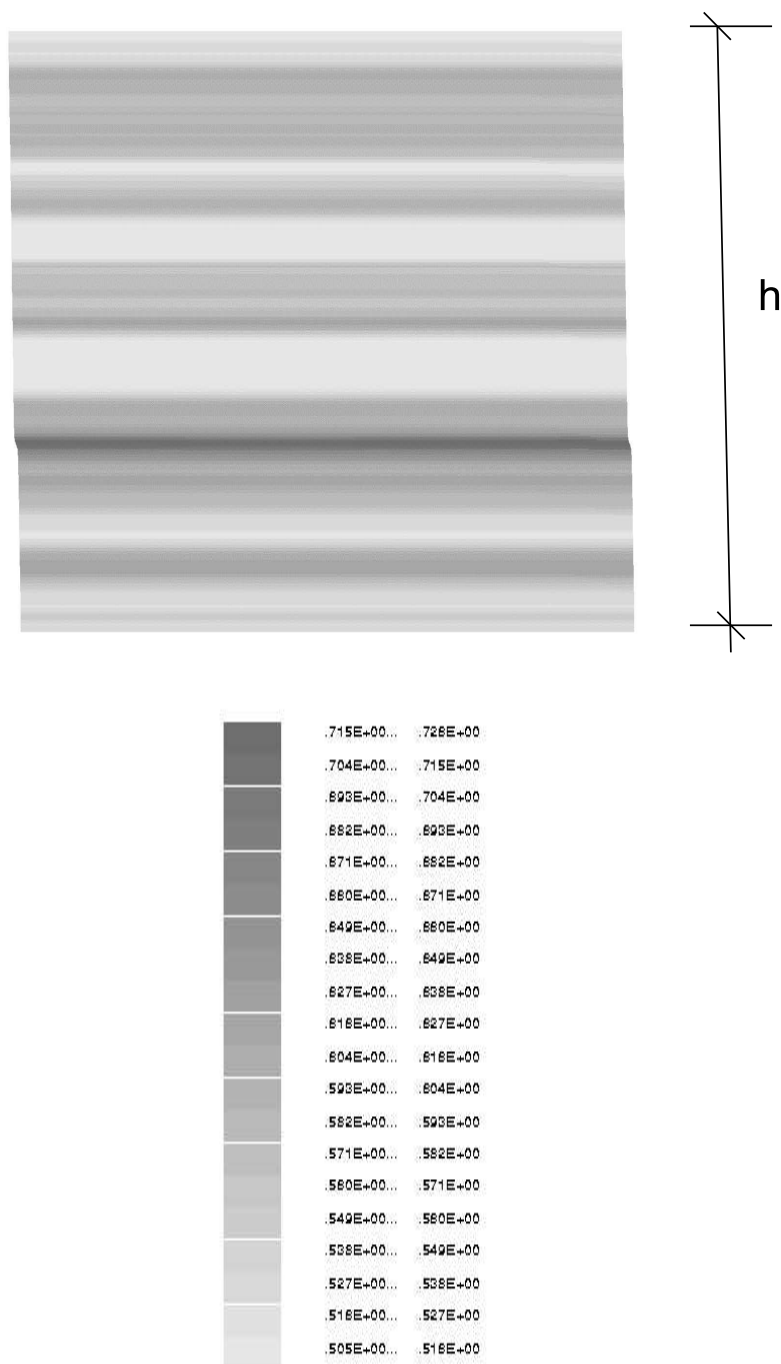


Fig. 10. Distribution of void ratio e during initial shearing with dense sand ($\bar{e}_o = 0.60$, $p = 200$ kPa), correlated random field of e_o , approach 'A', $s_d = 0.05$, $\lambda_{x2} = 1$, darker colour denotes an increase of e

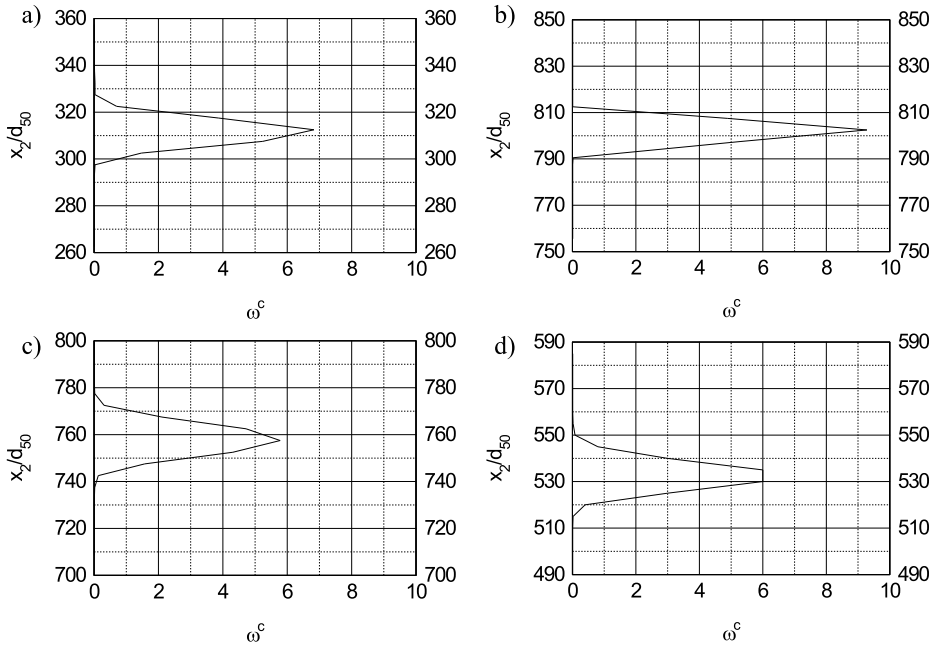


Fig. 11. Distribution of Cosserat rotation ω^c across the normalized height x_2/d_{50} in dense sand ($\bar{e}_o = 0.60$, correlated random field of e_o , approach 'A'): a) $s_d = 0.05$, $\lambda_{x2} = 1$, b) $s_d = 0.05$, $\lambda_{x2} = 3$, c) $s_d = 0.2$, $\lambda_{x2} = 1$, d) $s_d = 0.2$, $\lambda_{x2} = 3$

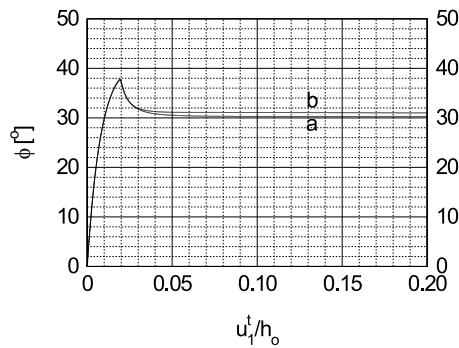


Fig. 12. Evolution of mobilized internal friction angle ϕ versus u_1^t/h_o during shearing with dense sand ($\bar{e}_o = 0.60$, correlated random field of e_o , approach 'B'): a) $s_d = 0.05$, $\lambda_{x1} = \lambda_{x2} = 1$, b) $s_d = 0.05$, $\lambda_{x1} = \lambda_{x2} = 3$



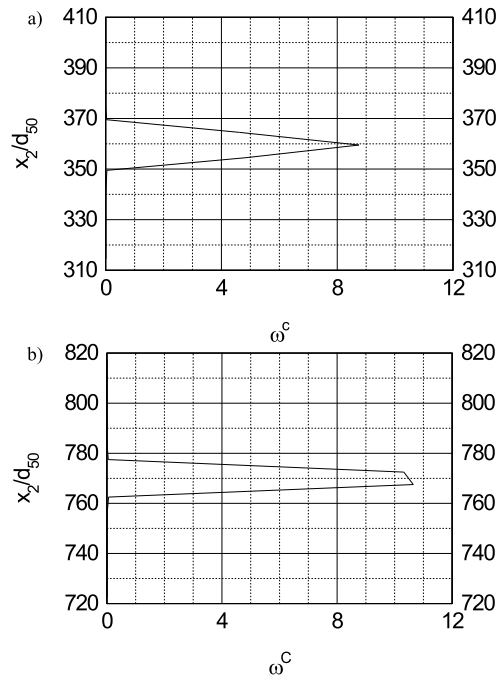


Fig. 13. Distribution of Cosserat rotation ω^c across the normalized height x_2/d_{50} in dense sand ($\bar{e}_o = 0.60$, correlated random field of e_o , approach 'B'): a) $s_d = 0.05$, $\lambda_{x1} = \lambda_{x2} = 1$, b) $s_d = 0.05$, $\lambda_{x1} = \lambda_{x2} = 3$

the approach 'A': $\phi_p = 37.8^\circ$ and $\phi_{res} = 30.3^\circ$ ($\lambda_{x1} = \lambda_{x2} = 1$, $s_d = 0.05$), and $\phi_p = 37.8^\circ$ and $\phi_{res} = 31.0^\circ$ ($\lambda_{x1} = \lambda_{x2} = 3$, $s_d = 0.05$), (Fig. 12). The thickness of the shear zone is smaller (Fig. 13): $20 \times d_{50}$ ($\lambda_{x1} = \lambda_{x2} = 1$, $s_d = 0.05$) and $15 \times d_{50}$ ($\lambda_{x1} = \lambda_{x2} = 3$, $s_d = 0.05$).

5.3. Non-correlated Random Fields of the Initial Void Ratio

Figs. 14–16 demonstrate the FE-results of shearing for single realizations with random fields of e_o generated by Eqs. 32 (Fig. 14), by Eq. 33 according to the Shahinpoor's (Shahinpoor 1981) idea (Fig. 15) and by a Gaussian function (Fig. 16), respectively.

Using random fields generated by Eq. 32, the mobilized internal friction angles are: $\phi_p = 41.5^\circ$ and $\phi_{res} = 30.3^\circ$ ($e_o = 0.55 + 0.1r$, approach 'A'), $\phi_p = 38.3^\circ$ and $\phi_{res} = 30.3^\circ$ ($e_o = 0.50 + 0.2r$, approach 'A'), $\phi_p = 44.0^\circ$ and $\phi_{res} = 31.0^\circ$ ($e_o = 0.55 + 0.1r$, approach 'B') and $\phi_p = 41.9^\circ$ and $\phi_{res} = 31.1^\circ$ ($e_o = 0.50 + 0.2r$, approach 'B'). The width of the shear zone is: $20 \times d_{50}$ ($e_o = 0.55 + 0.1r$, approach 'A'), $20 \times d_{50}$ ($e_o = 0.50 + 0.2r$, approach 'A'), $12 \times d_{50}$ ($e_o = 0.55 + 0.1r$, approach 'B') and $12 \times d_{50}$ ($e_o = 0.50 + 0.2r$, approach 'B').

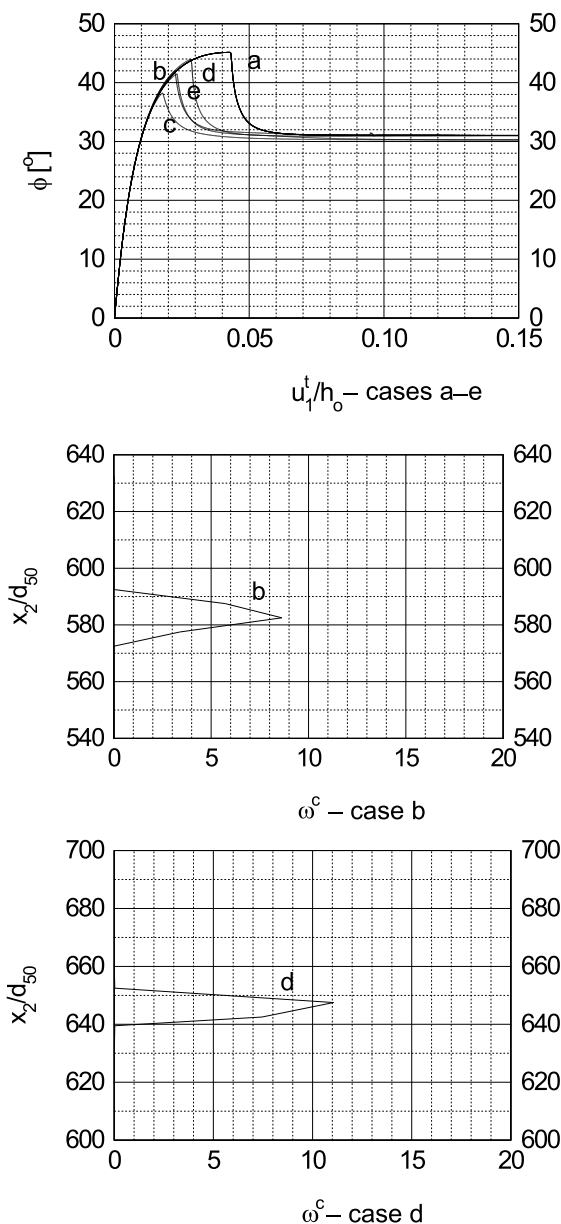


Fig. 14. Evolution of mobilized internal friction angle ϕ versus u_1^t/h_o and distribution of Cosserat rotation ω^c across the normalized height x_2/d_{50} during shearing with dense sand: a) $e_o = 0.60$, b) $e_o = 0.55 + 0.1r$ (approach 'A'), c) $e_o = 0.50 + 0.2r$ (approach 'A'), d) $e_o = 0.55 + 0.1r$ (approach 'B'), e) $e_o = 0.50 + 0.2r$ (approach 'B')

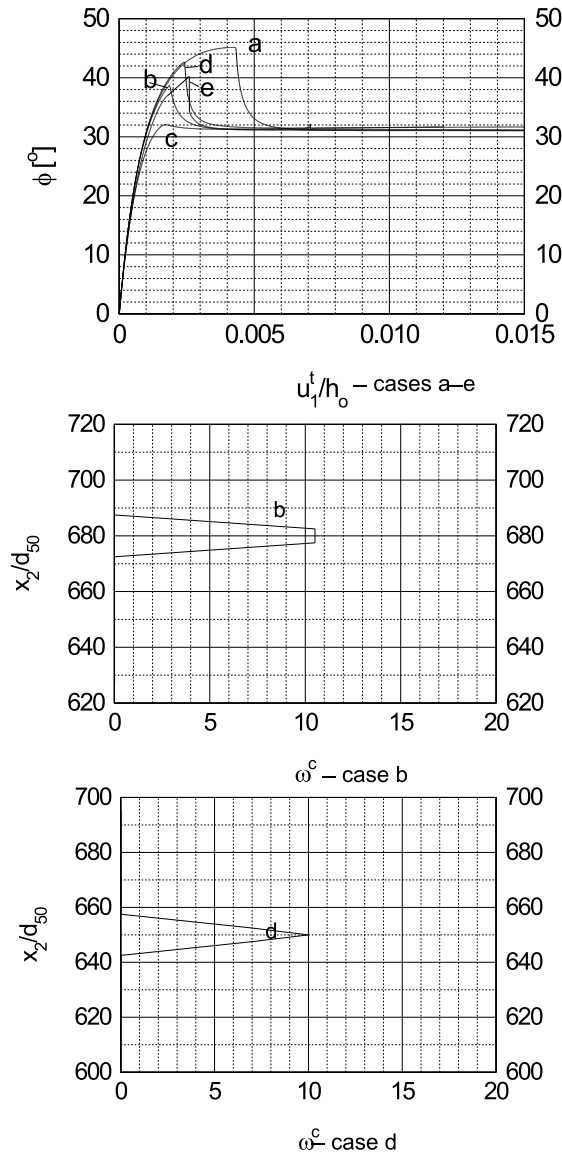


Fig. 15. Evolution of mobilized internal friction angle ϕ versus u_1^t/h_0 and distribution of Cosserat rotation ω^c across the normalized height x_2/d_{50} during shearing with dense sand: a) $e_o = 0.60$, b) Gaussian ($\bar{e}_o = 0.60$, $s_d = 0.05$, approach 'A'), c) Gaussian ($\bar{e}_o = 0.60$, $s_d = 0.2$, approach 'A'), d) Gaussian ($\bar{e}_o = 0.60$, $s_d = 0.05$, approach 'B'), e) Gaussian ($\bar{e}_o = 0.60$, $s_d = 0.2$, approach 'B')

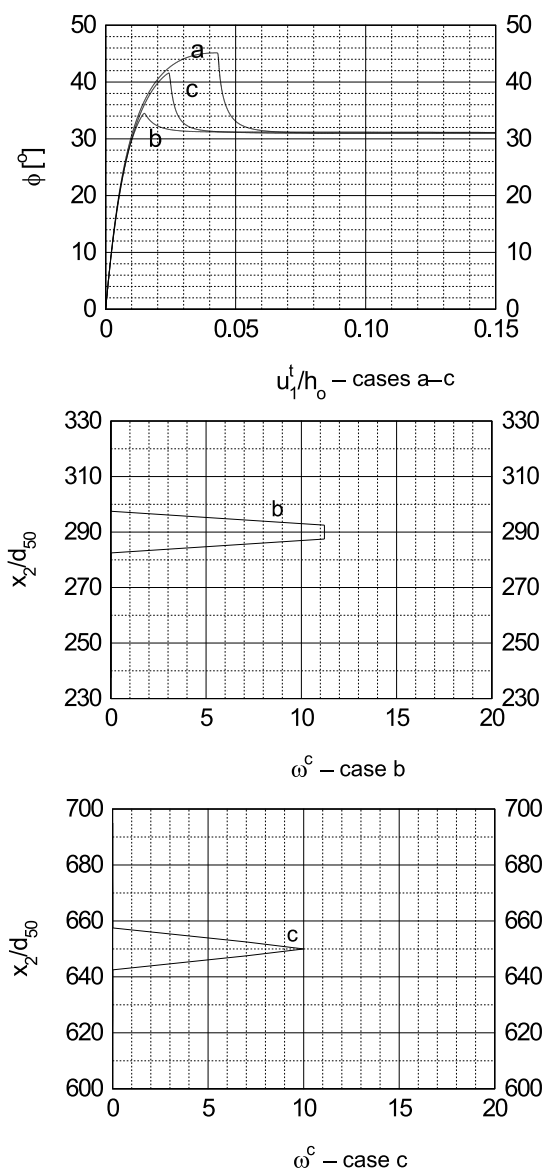


Fig. 16. Evolution of mobilized internal friction angle ϕ versus u_1^t/h_o and distribution of Cosserat rotation ω^c across the normalized height x_2/d_{50} during shearing with dense sand: a) $e_o = 0.60$, b) by Shahinpoor (1981) ($\bar{e}_o = 0.60$, approach 'A'), c) by Shahinpoor (1981) ($\bar{e}_o = 0.60$, approach 'B')



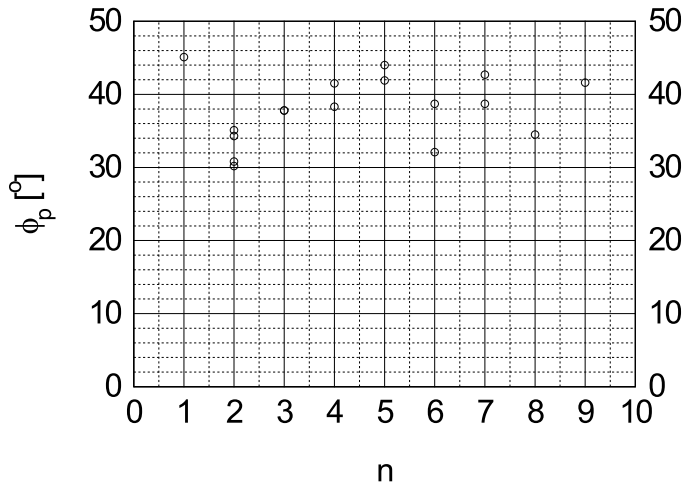


Fig. 17. Mobilized internal friction angles at peak ϕ_p for different distributions n of the initial void ratio e_o : $n = 1$ – uniform, $n = 2$ – correlated random field in the approach ‘A’, $n = 3$ – correlated random field in the approach ‘B’, $n = 4$ – non-correlated random field by Eq. 32 (approach ‘A’), $n = 5$ non-correlated random field by Eq. 32 (approach ‘B’), $n = 6$ – non-correlated random Gaussian field (approach ‘A’), $n = 7$ – non-correlated random Gaussian field (approach ‘B’), $n = 8$ – non-correlated random field by Shahinpoor (1981) (approach ‘A’), $n = 9$ – non-correlated random field by Shahinpoor (1981) (approach ‘B’)

In the case of random fields depicted with a Gaussian function, the mobilized internal friction angles are: $\phi_p = 38.7^\circ$ and $\phi_{res} = 31.0^\circ$ ($\bar{e}_o = 0.60$, $s_d = 0.05$, approach ‘A’), $\phi_p = 32.1^\circ$ and $\phi_{res} = 31.1^\circ$ ($\bar{e}_o = 0.60$, $s_d = 0.20$, approach ‘A’), $\phi_p = 42.7^\circ$ and $\phi_{res} = 31.6^\circ$ ($\bar{e}_o = 0.60$, $s_d = 0.05$, approach ‘B’) and $\phi_p = 38.7^\circ$ and $\phi_{res} = 31.0^\circ$ ($\bar{e}_o = 0.60$, $s_d = 0.20$, approach ‘B’). The width of the shear zone is: $15 \times d_{50}$ ($\bar{e}_o = 0.60$, $s_d = 0.05$, approach ‘A’), $15 \times d_{50}$ ($\bar{e}_o = 0.60$, $s_d = 0.20$, approach ‘A’), $10 \times d_{50}$ ($\bar{e}_o = 0.60$, $s_d = 0.05$, approach ‘B’) and $10 \times d_{50}$ ($\bar{e}_o = 0.60$, $s_d = 0.20$, approach ‘B’).

When the initial void ratio is distributed according to Eq. 33 (Shahinpoor 1981), the mobilized internal friction angles are: $\phi_p = 34.5^\circ$ and $\phi_{res} = 31.1^\circ$ ($\bar{e}_o = 0.60$, approach ‘A’) and $\phi_p = 41.6^\circ$ and $\phi_{res} = 31.0^\circ$ ($\bar{e}_o = 0.60$, approach ‘B’) with the shear zone thickness of $15 \times d_{50}$ ($\bar{e}_o = 0.60$, approaches ‘A’ and ‘B’).

The maximum friction angle is smaller than this with the uniform distribution of the initial void ratio. The results show that the larger the standard deviation s_d , the smaller t_s and ϕ_p . In the case of the horizontal non-uniformity of e_o , the maximum friction angle is higher and shear zone thickness is smaller.

The values of ϕ_p for different distributions of e_o are summarized in Fig. 17.

6. Conclusions

The following conclusions can be drawn on the initial FE-investigations of the effect of the distribution of the initial void ratio during shearing of an infinite granular layer:

- the thickness of the shear zone t_s at residual state increases with increasing initial void ratio e_o from $16 \times d_{50}$ up to $40 \times d_{50}$ in the range of $e_o = 0.60\text{--}0.80$ with the uniform distribution of the initial void ratio.
- The effect of the stochastic initial distribution of the initial void ratio significantly influences the maximum internal friction angle and the thickness of the shear zone. The residual friction angle remains the same.
- The shear resistance at peak is always smaller with the stochastic distribution of the initial void ratio as compared to this with the uniform one. Thus, the weakest link principle always applies here due to the shear localization forming in a horizontal weak layer.
- The shear resistance at peak is larger and the shear zone thickness is smaller when imperfections are taken into account also in a horizontal direction.
- For the spatial correlated distribution of e_o , the thickness of the shear zone, $t_s = (15 - 30) \times d_{50}$, can be significantly larger than this using the non-uniform distribution ($t_s = 16 \times d_{50}$). It is also generally larger to those obtained with the non-correlated distributions ($t_s = (12 - 20) \times d_{50}$).
- For the spatial correlated distribution of e_o , in general, the shear resistance at peak is smaller as compared with the non-correlated distributions.
- Several horizontal shear zones occur during initial shearing. Later, only one dominates.
- The shear resistance at peak and the thickness of the shear zone decrease with increasing standard deviation and decay coefficients.

It should be pointed out that the stochastic FE-analysis performed in this paper can only be considered as a preliminary one since only few samples have been calculated. It will be continued. Selected random fields will be chosen. The choice of the representative samples will be governed by the stratified or the Latin hypercube sampling method (Tejchman and Górski 2006). Thus, a statistical effect can be captured.

References

- Bauer E. (1996), Calibration of a comprehensive hypoplastic model for granular materials, *Soils and Foundations*, Vol. 36, No. 1, 13–26.
- Box G. E. P., Muller M. E. (1958), A note of the generation of random normal deviates, *Annals. Math. Stat.*, Vol. 29, 610–611.



- Cambou B., Dubujet P., Nougier C. (2004), Internal state in granular materials, [in:] *Modelling of Cohesive-Frictional Materials* (eds.: P. A. Vermeer, W. Ehlers, H. J. Herrmann and E. Ramm), Balkema, 13–25.
- Desrues J., Viggiani G. (2004), Strain localization in sand: overview of the experiments in Grenoble using stereophotogrammetry, *Int. J. Numer. Anal. Methods in Geomech.*, Vol. 28, No. 4, 279–321.
- Fenton G. A. (1999), Estimation for stochastic soil models, *J. Geotech. Geoenvironment. Eng.*, Vol. 125, No. 6, 470–485.
- Fenton G. A., Griffiths D. V. (2002), Probabilistic foundation settlement on spatially random soil, *J. Geotech. Geoenvironment. Eng.*, Vol. 128, No. 5, 381–389.
- Florian A. (1992), An efficient sampling scheme: Updated Latin hypercube sampling, *Probabilistic Engineering Mechanics*, No. 2, 123–130.
- Górski J. (2006), Non-linear models of structures with random geometric and material imperfections simulation-based approach, *Monography*, Gdańsk University of Technology, No. 68.
- Groen A. E. (1997), Three-dimensional elasto-plastic analysis of soils, *PhD Thesis*, Delft University, 1–114.
- Gudehus G. (1996), A comprehensive constitutive equation for granular materials, *Soils and Foundations*, Vol. 36, No. 1, 1–12.
- Gudehus G., Nübel K. (2004), Evolution of shear bands in sand, *Geotechnique*, Vol. 54, No. 3, 187–201.
- Gutierrez M. A., de Borst R. (1998), Energy dissipation, internal length scale and localization patterning – a probabilistic approach, [in:] *Computational Mechanics* (eds.: S. Idelsohn, E. Onate, E. Dvorkin), CIMNE, Barcelona, 1–9.
- Harris W. W., Viggiani G., Mooney M. A., Finno R. J. (1995), Use of stereophotogrammetry to analyze the development of shear bands in sand, *Geotechnical Testing Journal*, Vol. 18, No. 4, 405–420.
- Herle I., Gudehus G. (1999), Determination of parameters of a hypoplastic constitutive model from properties of grain assemblies, *Mechanics of Cohesive-Frictional Materials*, Vol. 4, No. 5, 461–486.
- Leśniewska D., Mróz Z. (2003), Shear bands in soil deformation processes, [in:] *Bifurcations and Instabilities in Geomechanics* (eds.: J. Labuz and A. Drescher), Swets and Zeitlinger, Lisse, 109–119.
- Maier T. (2002), Numerische Modellierung der Entfestigung im Rahmen der Hypoplastizität, *PhD Thesis*, University of Dortmund.
- Matthies H., Brenner C. E., Bucher C. G., Soares C. (1997), Uncertainties in probabilistic numerical analysis of structures and solids – stochastic finite elements, *Structural Safety*, Vol. 19, No. 3, 283–336.
- Niemunis A., Wichtmann T., Pietryna Y., Triantafyllidis T. (2005), Stochastic modelling of settlements due to cyclic loading for soil-structure interaction, *Proc. Int. Conf. Structural Damage and Lifetime Assessment*, Rome, 1–8.
- Nübel K. (2002), Experimental and numerical investigation of shear localisation in granular materials, *Publication Series of the Institute of Soil and Rock Mechanics*, University Karlsruhe, No. 62.
- Nübel K., Karcher Ch. (1998), FE simulations of granular material with a given frequency distribution of voids as initial condition, *Granular Matter*, Vol. 1, No. 3, 105–112.
- Oda M. (1993), Micro-fabric and couple stress in shear bands of granular materials, [in:] *Powders and Grains* (ed.: C. Thornton), Rotterdam, Balkema, 161–167.
- Pasternak E., Mühlhaus H.-B. (2001), Cosserat continuum modelling of granulate materials, [in:] *Computational Mechanics – New Frontiers for New Millennium* (eds.: S. Valliappan S. and N. Khalili), Elsevier Science, 1189–1194.

- Pena A. A., Herrmann H. J., Lizcano A., Alonso-Marroquin F. (2005), Investigation of the asymptotic states of granular materials using a discrete model of anisotropic particles, [in:] *Powders and Grains* (eds.: Garcia-Rojo R., Herrmann H. J., McNamara S.), Taylor and Francis Group, London, 697–700.
- Przewłócki J., Górski J. (2001), Strip foundation on 2-D and 3-D random subsoil, *Probabilistic Engineering Mechanics*, No. 16, 121–136.
- Rechenmacher A. L. (2006), Grain-scale processes governing shear band initiation and evolution of sands, *J. Mechanics and Physics of Solids*, No. 54, 22–45.
- Rechenmacher A. L., Finno R. J. (2003), Shear band displacements and void ratio evolution to critical state in dilative sand, [in:] *Bifurcation and Instabilities in Geomechanics* (eds.: J. Labuz and A. Drescher), Swets and Zeitlinger, Lisse, 193–205.
- Rechenmacher A. L., Finno R. J. (2004), Digital Image Correlation to evaluate shear banding in dilative sands, *Geotechnical Testing Journal*, Vol. 27, No. 1, 13–22.
- Rubinstein R. Y. (1981), *Simulation and the Monte Carlo method*, New York, J. Wiley & Sons.
- Schäfer H. (1962), Versuch einer Elastizitätstheorie des zweidimensionalen ebenen Cosserat-Kontinuums, *Miszellaneen der Angewandten Mechanik*, Festschrift Tolmien, W., Berlin, Akademie-Verlag.
- Shahinpoor M. (1981), Statistical mechanical considerations on storing bulk solids, *Bulk Solid Handling*, Vol. 1, No. 1, 31–36.
- Sheppard A., Knackstedt M., Senden T., Saadatfar M. (2006), Analysis of granular materials using X-ray micro-CT, *Proc. 20th Canberra International Summer School and Workshop on Granular Material*, 53–53.
- Ślomiński C., Niedostatkiewicz M., Tejchman J. (2006), Deformation measurements in granular bodies using a Particle Image Velocimetry technique, *Archives of Hydro-Engineering and Environmental Mechanics* (in print).
- Tejchman J. (1989), Scherzonenbildung und Verspannungseffekte in Granulatem unter Berücksichtigung von Korndrehungen, *Publication Series of the Institute of Soil and Rock Mechanics*, University Karlsruhe, No. 117, 1–236.
- Tejchman J. (2004a), Influence of a characteristic length on shear zone formation in hypoplasticity with different enhancements, *Computers and Geotechnics*, Vol. 31, No. 8, 595–611.
- Tejchman J. (2004b), FE-analysis of patterning of shear zones in granular bodies for earth pressure problems of a retaining wall, *Archives of Hydro-Engineering and Environmental Mechanics*, Vol. 51, No. 4, 317–348.
- Tejchman J. (2006), Effect of fluctuation of current void ratio on the shear zone formation in granular bodies within micro-polar hypoplasticity, *Computers and Geotechnics*, Vol. 33, No. 1, 29–46.
- Tejchman J., Bauer E. (1996), Numerical simulation of shear band formation with a polar hypoplastic model, *Computers and Geotechnics*, Vol. 19, No. 3, 221–244.
- Tejchman J., Górski J. (2006), Effect of a spatially distribution random distribution of initial void ratio on shear zone formation, *Proc. 35th Int. Solid Mechanics Conference Solmech*, Krakow, 4–8.09.2006, 31–32.
- Tejchman J., Gudehus G. (2001), Shearing of a narrow granular strip with polar quantities, *J. Num. and Anal. Methods in Geomechanics*, No. 25, 1–18.
- Tejchman J., Niemunis A. (2006), FE-studies on shear localization in an anisotropic micro-polar hypoplastic granular material, *Granular Matter*, Vol. 8, No. 3–4, 205–220.
- Vardoulakis I. (1980), Shear band inclination and shear modulus in biaxial tests, *Int. J. Num. Anal. Meth. Geomech.*, No. 4, 103–119.



- Vorechovsky M., Matesova D. (2006), Size effect in concrete specimens under tension: interplay of sources, [in:] *Computational Modelling of Concrete Structures, EURO-C* (eds.: G. Meschke, R. de Borst, H. Mang and N. Bicanic), Taylor and Francis, 905–914.
- Walukiewicz H., Bielewicz E., Górski J. (1997), Simulation of nonhomogeneous random fields for structural applications, *Computers and Structures*, Vol. 64, No. 1–4, 491–498.
- Wang C. C. (1970), A new representation theorem for isotropic functions. *J. Rat. Mech. Anal.*, No. 36, 166–223.
- Wolffersdorff P. A. von (1996), A hypoplastic relation for granular materials with a predefined limit state surface, *Mechanics Cohesive-Frictional Materials*, No. 1, 251–271.
- Yoshida Y., Tatsuoka T., Siddiquee M. S. (1994), Shear banding in sands observed in plane strain compression, [in:] *Localisation and Bifurcation Theory for Soils and Rocks*, (eds.: R. Chambon, J. Desrues and I. Vardoulakis), Balkema, Rotterdam, 165–181.